PAPER

Check for updates

Atomic layer deposition of PbCl$_2$, PbBr$_2$ and mixed lead halide (Cl, Br, I) PbX$_n$Y$_{2-n}$ thin films†

Georgi Popov, [ID] *[a] Goran Bačić, [ID] [b] Charlotte Van Dijck,[a] Laura S. Junkers, [ID] [a]
Alexander Weiß, [ID] [a] Miika Mattinen, [ID] [a] Anton Vihervaara, [ID] [a]
Mykhailo Chundak, [ID] [a] Pasi Jalkanen, [ID] [c] Kenichiro Mizohata, [ID] [c]
Markku Leskelä, [ID] [a] Jason D. Masuda, [ID] [d] Seán T. Barry, [ID] [b] Mikko Ritala [ID] *[a] and
Marianna Kemell [ID] [a]

Atomic layer deposition offers outstanding film uniformity and conformality on substrates with high aspect ratio features. These qualities are essential for mixed-halide perovskite films applied in tandem solar cells, transistors and light-emitting diodes. The optical and electronic properties of mixed-halide perovskites can be adjusted by adjusting the ratios of different halides. So far ALD is only capable of depositing iodine-based halide perovskites whereas other halide processes are lacking. We describe six new low temperature (≤100 °C) ALD processes for PbCl$_2$ and PbBr$_2$ that are crucial steps for the deposition of mixed-halide perovskites with ALD. Lead bis[bis(trimethylsilyl)amide]−GaCl$_3$ and −TiBr$_4$ processes yield the purest, crystalline, uniform and conformal films of PbCl$_2$ and PbBr$_2$ respectively. We show that these two processes in combination with a PbI$_2$ process from the literature deposit mixed lead halide films. The four less optimal processes revealed that reaction by-products in lead halide deposition processes may cause film etching or incorporate themselves into the film.

1. Introduction

This work describes new atomic layer deposition (ALD) processes for lead chloride and bromide thin films. These halide thin films act as precursors for halide perovskite thin films.[1] Halide perovskites are a group of compounds with a crystal structure similar to the mineral perovskite and the general formula ABX$_3$, where A is typically an amine or caesium, B is lead or tin, and X is a halide, namely chloride, bromide or most commonly iodide. Halide perovskites possess remarkable optoelectronic properties and have rapidly established themselves as the next generation photovoltaic materials.[2,3] However, the potential of halide perovskites is not limited to photovoltaics.[4] At present, they display impressive perform-

ance in many devices[5] including light-emitting diodes (LEDs),[6] X-ray scintillators[7] and transistors.[8]

We believe that in certain applications ALD can become the method of choice for depositing halide perovskites. ALD offers uniformity and conformality that other deposition methods struggle to achieve. These advantages allow ALD to excel in applications, such as microelectronics, that rely on complex high aspect ratio structures.[9] In the halide perovskite case, high aspect ratio structures either enable key functionality of the device or enhance performance.[5]

Previously we have developed ALD processes for PbI$_2$[10] and CsI[11] based on metal bis(trimethylsilyl)amides (btsa) and tin tetraiodide. In these processes a ligand exchange reaction between the metal (btsa) and SnI$_4$ yields the desired metal iodide and volatile heteroleptic tin by-products (Sn(btsa)$_x$I$_{4-x}$). The PbI$_2$ and CsI processes also allowed us to deposit thin films of CH$_3$NH$_3$PbI$_3$ (MAPbI$_3$)[10] and CsPbI$_3$.[11] However, most halide perovskite applications rely on mixed halide perovskites *i.e.*, partial substitution of ions in the perovskite composition, for example substitution of iodine with bromine or chlorine in MAPbI$_3$.[5–8,12] Currently (June 2022), to our knowledge, our iodide ALD processes,[10,11] the work of Natarajan *et al.* on copper chloride[13] as well as the recent work of Vagott *et al.* on PbI$_2$[14] constitute the entirety of existing literature on direct ALD of metal chlorides and iodides.[15] No metal bromide ALD

[a]Department of Chemistry, University of Helsinki, P. O. Box 55, FI-00014 Helsinki, Finland. E-mail: georgi.popov@helsinki.fi, mikko.ritala@helsinki.fi
[b]Department of Chemistry, Carleton University, 1125 Colonel By Drive, Ottawa, Ontario K1S 5B6, Canada
[c]Department of Physics, University of Helsinki, P. O. Box 43, FI-00014 Helsinki, Finland
[d]Department of Chemistry, Saint Mary's University, 923 Robie Street, Halifax, Nova Scotia B3H 3C3, Canada
†Electronic supplementary information (ESI) available. CCDC 2180984. For ESI and crystallographic data in CIF or other electronic format see DOI: https://doi.org/10.1039/d2dt02216h

processes have been reported. This work expands the range of metal halides that can be deposited with ALD to lead chloride and bromide.

We hypothesized that the chemistry that we used for iodides is straightforward to extend to chlorides and bromides, but we encountered a number of challenges and a chloride process required a previously unthought halide precursor. The use of metal halide as a halide precursor originates from the metal fluoride ALD chemistry developed by Pilvi *et al.* who used TiF_4 and TaF_5 as fluorine precursors. In the fluoride ALD process the use of metal fluorides as fluorine sources allows to avoid the use of anhydrous HF gas. In our case, the lack of commercial availability of the anhydrous HCl, HBr and HI gases compelled us to investigate alternatives like the use of metal halides as halide precursors. The technical challenges we faced originated from the halide precursors. Tin(IV) iodide is a convenient iodide precursor for the metal iodide deposition, but the analogous chloride and bromide had either performance or delivery issues. To circumvent these issues, we studied alternative halide precursors: titanium(IV) halides and gallium(III) chloride as well as an alternative lead precursor: bis[lead(II) *N,N′*-di-*tert*-butyl-1,1-dimethylsilanediamide] ([Pb (gem)]$_2$). Here, we describe these studies and their outcome: ALD processes for $PbCl_2$ and $PbBr_2$. Both processes use Pb (btsa)$_2$ as the lead precursor, whereas $GaCl_3$ and $TiBr_4$ are the respective halide precursors.

2. Results and discussion

Table 1 shows key characteristics of the processes we studied. Pb(btsa)$_2$ combined with either $GaCl_3$ or $TiBr_4$ result in good processes whereas the other chemistries either lack key ALD characteristics or deposit thin films with undesired properties.

2.1 Pb(btsa)$_2$–SnCl$_4$ process

At 65 °C, Pb(btsa)$_2$ and $SnCl_4$ yielded crystalline and pure $PbCl_2$ (Fig. S1a and b,† refractive index 2.3, literature value 2.3 [16]), but the films suffered from severe thickness non-uniformity (Fig. S1c†). Standard deviations in thickness across the substrate (σ_d) ranged from 14 to 88%. The films were thinner at the precursor inlet edge of the substrate and most uniform

films required short pulse durations with no purge in between (Fig. S1d†). Long pulse or purge durations as well as higher deposition temperatures caused an expansion of the thinner region across the substrate and ultimately no deposition at all (Fig. S1e–h†).

Our experimental results suggested that an intermediate product with the formula $Sn(btsa)_x(Cl)_{4-x}$ of the reaction between Pb(btsa)$_2$ and $SnCl_4$ was responsible for the etching rather than the precursors themselves. Neither Pb(btsa)$_2$ or $SnCl_4$ pulsed onto an already deposited $PbCl_2$ film (2000 cycles at 65 °C, precursor pulse and purge durations were 1 and 3 s respectively) caused any measurable decrease in the film thickness or change in the thickness profile. Additionally, sublimation of $PbCl_2$ could not explain the etching as other processes can deposit $PbCl_2$ films that are stable inside our reactors up to at least 135 °C. These observations were further supported by a quantum chemical study (*vide infra*) presented in Section 2.5.

2.2 Pb(btsa)$_2$–TiCl$_4$ process

Because $SnCl_4$ did not yield a good process we turned to $TiCl_4$ as a next possible chloride precursor. Tetrahalides (Cl, Br, I) of tin and titanium have similar structure, size, and properties, although titanium tetrahalides are slightly less volatile than the tin analogues.

The thinning effect observed with $SnCl_4$ did not occur in the case of $TiCl_4$. On the contrary the films were thicker at the precursor inlet edge with a visible thickness gradient (σ_d = 40%). Short pulse and long purge durations as well as a thin ALD Al_2O_3 underlayer (2 nm) deposited with trimethylaluminum (TMA) and H_2O, improved the thickness uniformity (Fig. S2a and d†).

Key ALD characteristics were missing from the Pb(btsa)$_2$ and $TiCl_4$ process. The growth per cycle (GPC) saturated with respect to the $TiCl_4$ pulse and purge durations but not with respect to the Pb(btsa)$_2$ pulse durations (Fig. S2c and d†). At the deposition temperature of 75 °C the thickness increased linearly with the increasing number of deposition cycles (Fig. S2f†). The GPC decreased with increasing deposition temperature (Fig. S2g†).

The films are not pure $PbCl_2$ and are chlorine deficient (Fig. S2h†). Titanium and oxygen are present in significant amounts, whereas carbon and nitrogen are not. Changes in

Table 1 Overview of processes studied in this work

Material	Lead precursor	Halide precursor	Crystallinity	Metal impurities	Refractive index[a]	Process characteristics
$PbCl_2$	Pb(btsa)$_2$	$SnCl_4$	Crystalline	<0.1 at% Sn	2.3	No saturation, etching
		$TiCl_4$	Crystalline	11.2 at% Ti	1.9	Saturation with respect to the halide precursor but not the metal precursor
		$GaCl_3$	Crystalline	1.0 at% Ga	2.2	Saturation
	(Pb(gem))$_2$	$SnCl_4$	Crystalline	15.9 at% Sn	1.9	Saturation
$PbBr_2$	Pb(btsa)$_2$	$SnBr_4$	Amorphous	7.8 at% Sn	1.9	Saturation with respect to the halide precursor but not the metal precursor
		$TiBr_4$	Crystalline	0.5 at% Ti	2.5	Saturation

[a] At 580 nm.

process parameters did not yield any significant changes in film composition. No well-defined grains or grain boundaries are visible with FESEM (Fig. S2b†). XRD reveals $PbCl_2$ reflections (FWHM 0.5° of 2θ) for the 30–80 nm thick films deposited in the 65–110 °C temperature range (Fig. S2i†). The measured refractive index (1.9) does not match that of $PbCl_2$ (2.3 [16]).

We speculate that the formation of a ternary chloride, for instance $PbTiCl_6$, along with $PbCl_2$ can explain the impurity and poor crystallinity of the films. The Pb : Ti : O ratio is roughly 1 : 1 : 3 if we subtract the $PbCl_2$ part from the composition given in Fig. S2h.† Only $PbCl_2$ reflections are present in the XRD patterns, therefore the oxygen containing part of the film likely consists of one or more of the amorphous phases of PbO, TiO_2 and $PbTiO_3$. The oxygen containing part can form when the ternary chloride is exposed to ambient air (eqn (1) and (2)).
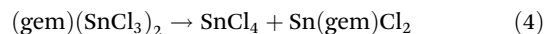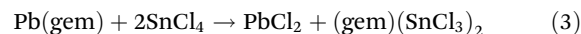
$$PbTiCl_6(s) + 3H_2O(g) \rightarrow PbO(s) + TiO_2(s) + 6HCl(g) \quad (1)$$

$$PbTiCl_6(s) + 3H_2O(g) \rightarrow PbTiO_3(s) + 6HCl(g) \quad (2)$$
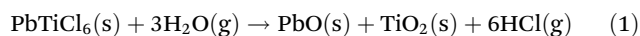
Literature covers many ternary fluoride II–IV compounds with double ReO_3 type (DROT) perovskite structure[17] as well as some II–IV chlorides with various structures.[18–20] Alternatively, one or more air sensitive and non-volatile Pb and Ti containing by-products can account for the observed oxygen containing composition.

2.3 $(Pb(gem))_2$–$SnCl_4$ process

$(Pb(gem))_2$ is a new precursor for the ALD field. $(Pb(gem))_2$ has excellent thermal stability up to at least 300 °C[21] and is more volatile than $Pb(btsa)_2$ (Fig. 1 and Fig. S3†). These properties make $(Pb(gem))_2$ usable in a wide temperature range. Wrackmeyer *et al.* describe that in solution Pb(gem) and $SnCl_4$ react to form $PbCl_2$ and $Sn(gem)Cl_2$ (eqn (3) and (4)),[22] which

encouraged us to explore the same chemistry in ALD. We also speculated that avoiding the (btsa) ligand would allow us to circumvent the etching issue in the $Pb(btsa)_2$–$SnCl_4$ process.

$$Pb(gem) + 2SnCl_4 \rightarrow PbCl_2 + (gem)(SnCl_3)_2 \quad (3)$$

$$(gem)(SnCl_3)_2 \rightarrow SnCl_4 + Sn(gem)Cl_2 \quad (4)$$

The films deposited with the $(Pb(gem))_2$–$SnCl_4$ process had a visible thickness gradient. The thickness decreased in the direction of the precursor flow (Fig. S4a†). The thickness gradient was observed at all deposition temperatures but varied in steepness. This change in steepness caused notable scatter in the GPC *vs.* deposition temperature data (Fig. S4c†). Assuming this scatter does not obscure the trend in GPC, the GPC is constant up to 135 °C. No deposition occurs at temperatures above 135 °C. At 85 °C the GPC saturates with respect to both precursor pulse durations but increases with increasing purge duration (Fig. S4d–f†). The film thickness depends linearly on the number of deposition cycles (Fig. S4g†).

The films made from $(Pb(gem))_2$ and $SnCl_4$ contained significant amounts of tin, oxygen, carbon and hydrogen (Fig. S4h†), but the Pb to Cl ratio was nevertheless 1 to 2. The films were amorphous at deposition temperatures below 85 °C, whereas broad (FWHM 1.0° of 2θ) $PbCl_2$ reflections appeared at 85 °C and higher deposition temperatures (Fig. S4i†). FESEM images show small grains embedded in a featureless matrix (Fig. S4b†). The measured refractive index (1.9) differs significantly from the literature value for $PbCl_2$ (2.3, ref. 16).

The composition of the films made with the $(Pb(gem))_2$–$SnCl_4$ process suggests that the source of the impurities is a different one than in the $Pb(btsa)_2$–$TiCl_4$ process. The notable Sn, O, and H contents as well as the Pb to Cl ratio matching stoichiometric $PbCl_2$ may indicate that by-products, which contain the (gem) ligand (see eqn (3) and (4)), are incorporated

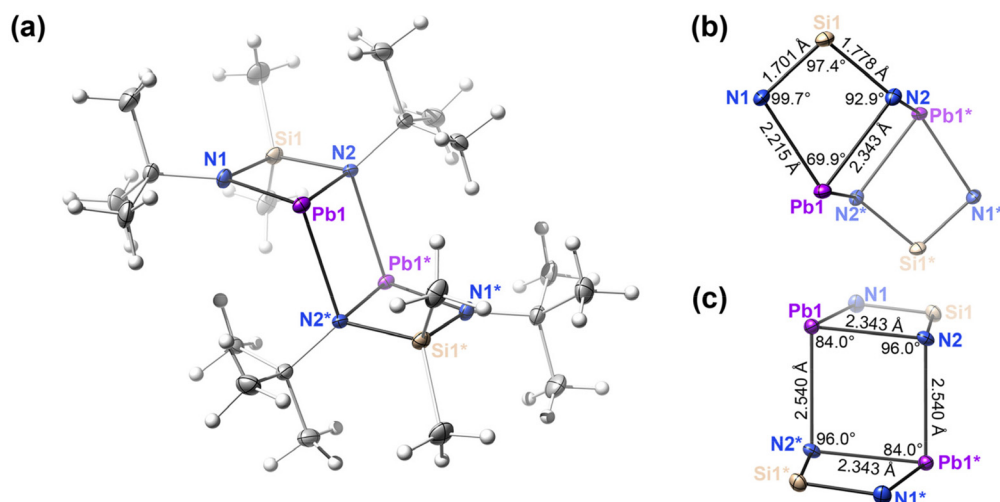**Fig. 1** (a) Asymmetric unit of $(Pb(gem))_2$ in the solid state as determined by single-crystal X-ray diffraction (scXRD), (b and c) interatomic distances and angles of the central inorganic ladderane structure with carbons and hydrogens omitted for clarity. Ellipsoids were drawn at the 50% probability isosurface, except hydrogens which were drawn as spheres.

into the film during deposition. The reason for the by-product incorporation could be their insufficient volatility in the temperature range where the $PbCl_2$ deposition occurs. The oxygen content can be attributed to the reaction of these incorporated by-products with ambient air.

To summarize, $(Pb(gem))_2$ offers many advantages over Pb $(btsa)_2$, such as simpler synthesis, better storage and thermal stability.[21,23] But these advantages cannot be exploited when $(Pb(gem))_2$ is paired with $SnCl_4$ to deposit $PbCl_2$. For instance, the remarkable thermal stability which $(Pb(gem))_2$ exhibits up to 300 °C, has no importance since deposition only occurs at temperatures below 135 °C. Furthermore, $(Pb(gem))_2$ and $SnCl_4$ generate non-volatile by-products (eqn (3) and (4)),[22] that negatively affect film qualities such as thickness uniformity, purity and crystallinity (Fig. S4a, h and i†). Nevertheless, $(Pb(gem))_2$ could still be a viable alternative for the deposition of lead compounds if paired with co-reactants that do not generate non-volatile by-products.

2.4 Pb(btsa)$_2$–GaCl$_3$ process

We investigated other metal chlorides as possible chlorine precursors because of the issues we observed with $SnCl_4$ and $TiCl_4$. $GaCl_3$ stood out in our literature study. Several studies describe $GaCl_3$ as a volatile gallium precursor that can be used in ALD of gallium compounds.[24–26] Reports on $GaCl_3$ reacting with metal bis(trimethylsilyl)amides to form the corresponding metal chloride and volatile by-products were also promising.[27–30]

Delivery of $GaCl_3$ required some creativity. Typically, in our F120 ALD reactors, volatile solids are delivered from open glass boats that are placed inside the reactor and heated to the source temperature. The volatility of $GaCl_3$, however, allowed its delivery at room temperature, *i.e.* without additional heating. Films deposited with $GaCl_3$ delivered from an open glass boat, that we use for solid precursors, were rough with nonuniform thickness (Fig. S5a†). Despite these detrimental features the gallium content in the films was small (<2 at%, EDS).

We suspected that the poor quality of the films was caused by overdosing of $GaCl_3$ as well as incomplete purging. $GaCl_3$ consumption was thrice as high than the typical precursor consumption in our reactors. Longer purge durations and higher deposition temperature slightly improved the uniformity. Normally the next step would be to lower the precursor source temperature, but $GaCl_3$ was already being delivered without heating. Instead, we attempted to lower $GaCl_3$ dose by limiting its flow out of the glass boat with an orifice. A 7 × 5 mm orifice decreased the thickness non-uniformity (σ_d) to 26% (Fig. S5b and S6a†). While this improvement was significant, the thickness non-uniformity was still exceeded what we consider acceptable for our flow-type reactors ($\sigma_d \leq 5\%$). Even smaller orifice sizes would, however, imped the loading of solid $GaCl_3$. To overcome this obstacle, we used $GaCl_3$ solution instead of the solid $GaCl_3$. Dissolving $GaCl_3$ allowed it's loading *via* a syringe and further reduction of the size of the orifice down to 1 mm. Hexane was the solvent of choice, as it

is inert towards $GaCl_3$ and evaporates during the reactor pump down, leaving solid $GaCl_3$ in the source boat (Video S1†).

With an optimized $GaCl_3$ delivery system the films were uniform (σ_d = 4.6%, Fig. S5c and S6b†) and the $Pb(btsa)_2$–$GaCl_3$ process had the characteristics typical for an ALD process. Deposition of $PbCl_2$ occurred in the 65–145 °C temperature range. There is no deposition temperature range where the GPC is constant, but only slight GPC changes occur between 65 and 105 °C (Fig. 2a). At 85 °C, the GPC saturates with respect to both precursor pulse durations and is independent of the purge durations, provided they are long enough (Fig. 2b–e). The film thickness at 85 °C increases linearly with an increasing number of cycles, apart from an initial steeper slope, that can be attributed to enhanced nucleation on Si (Fig. 2f).

The films are crystalline $PbCl_2$ at all deposition temperatures (Fig. 3a and Fig. S7†). No impurity phases were observed in XRD patterns and Raman spectra of the films (Fig. 3b). Composition analysis with ToF-ERDA shows that the films contain only 1.0 at% gallium as well as some oxygen, hydrogen and traces of nitrogen and carbon (Fig. S8†). The oxygen is concentrated at the film surface and is likely present due to the exposure of the samples to ambient air. This is underpinned by a pungent smell in the containers used for storing $PbCl_2$ films for prolonged times and the observation of opaqueness and minor discoloration of a $PbCl_2$ film after it was stored in ambient conditions (Fig. S9a†). EDS of the air-stored sample showed increased oxygen content, whereas XRD only showed a slight decrease in the intensity of the $PbCl_2$ reflections and no impurity phases (Fig. S9b and c†). Therefore, inert storage conditions are needed to prevent degradation of the $PbCl_2$ films.

X-ray photoelectron spectroscopy (XPS) spectra show the same elements as ToF-ERDA (Fig. S10a†) with Pb and Cl being the main constituents. The Pb 4f spectrum consists of two doublets (Fig. S10b†). The higher intensity doublet at 139.2 and 144 eV corresponds to $PbCl_2$ [31] and the lower intensity one at 136.9 eV and 141.7 eV to metallic Pb^0.[32] Literature is scarce on degradation and XPS studies of binary lead compounds but in the studies on lead halide perovskites, Pb^0 was commonly observed and associated with Pb^0 defect clusters induced by degradation of the compound in ambient air.[33–37] Cl 2p spectrum consists of a single doublet corresponding to $PbCl_2$ (Fig. S10c†).[38] Ga 2p spectrum also consists of a single doublet corresponding to Ga_2O_3 (Fig. S10d†).[39,40] $GaCl_3$ is hygroscopic and in ambient air reacts with H_2O to form Ga_2O_3 and HCl.[41] Gallium containing by-products formed in the ALD processes are expected to react similarly. Therefore, Ga_2O_3 most likely originates from either $GaCl_3$ or by-products incorporated into the film during the deposition that subsequently reacted with moisture upon exposure to ambient air. The O 1s spectrum consists of four peaks dominated by contaminants accumulated on the film surface from ambient air (Fig. S10e†). These peaks can be tentatively assigned as follows: at 531.2 eV to Ga_2O_3 and organic carbon contaminants, 532.2 eV to OH

Fig. 2 Growth per cycle (GPC) of $PbCl_2$ on silicon as a function of (a) deposition temperature, (b) $Pb(btsa)_2$ pulse duration, (c) $GaCl_3$ pulse duration, (d) purge duration after $Pb(btsa)_2$ pulse and (e) purge duration after $GaCl_3$ pulse. (f) $PbCl_2$ film thickness as a function of deposition cycles. Unless otherwise evident the depositions were made at 85 °C, with 600 cycles of 1.5 s $Pb(btsa)_2$ pulse, 0.8 s $GaCl_3$ pulse and 3.0 s purge durations. Thicknesses were measured with ellipsometry.
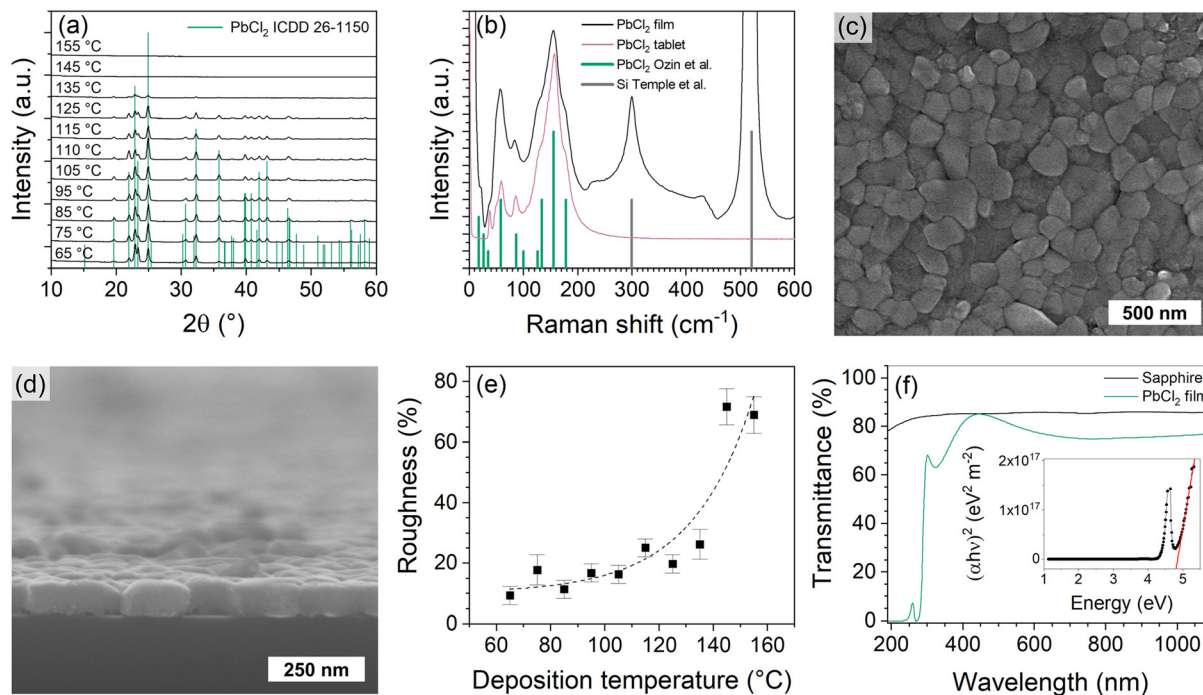

Fig. 3 (a) XRD patterns of $PbCl_2$ films deposited at different temperatures. Enlarged and indexed XRD patterns are shown in Fig. S7.† (b) Raman spectra of a $PbCl_2$ film on a thermal SiO_2/Si substrate and of a tablet pressed from commercial $PbCl_2$ powder (99.999%, Alfa Aesar). The $PbCl_2$ film was deposited with 1200 cycles. Literature patterns for $PbCl_2$[78] and Si[79] are shown for reference. FESEM image of a $PbCl_2$ film taken (c) top-down and (d) from cross-section. (e) $PbCl_2$ film roughness relative to the thickness as a function of deposition temperature. (f) Transmittance of a $PbCl_2$ film deposited on sapphire and of a bare sapphire wafer as reference. Inset shows the Tauc plot constructed from the transmittance spectrum of the $PbCl_2$ film in (f). The extra features in the transmittance spectrum and the peak in the Tauc plot at 4.5 eV are caused by interference in the film. See Fig. S12† for more details. Unless otherwise evident the depositions were made at 85 °C, with 600 cycles of 1.5 s $Pb(btsa)_2$ pulse, 0.8 s $GaCl_3$ pulse and 3.0 s purge durations.

groups, 533 eV to organic carbon contaminants and 534.1 eV to H_2O.[39,42]

PbCl$_2$ films consist of columnar grains (Fig. 3c and d). With the same number of deposition cycles, the size of the grains decreases with increasing deposition temperature (Fig. S11†). An 85 nm thick PbCl$_2$ film deposited at 85 °C had a surface roughness (R_q) of 10 nm, which is 12% of the film thickness. Such roughness is typical for crystalline metal halide films deposited with ALD.[10,11] As the deposition temperature increases the relative roughness starts to increase exponentially, because the GPC decreases, causing films deposited with the same number of cycles to become thinner and discontinuous (Fig. 3e).

The optical properties of the PbCl$_2$ films are in good agreement with the literature. The films are transparent in the visible range and absorb in the UV range (Fig. 3f and Fig. S12†). The optical band-gap, extracted from the Tauc plot (Fig. 3f, inset), is 4.9 eV (lit. 4.7–4.9 eV)[43–46] and the refractive index of the films was 2.2 (lit. 2.3).[16]

PbCl$_2$ film grew conformally on a patterned Si substrate without any additional optimization of the process parameters (Fig. 4). The film was smooth and consisted of columnar grains similar to the ones observed on the planar Si substrate (Fig. 3c and d).

Fig. 4 FESEM image of a PbCl$_2$ film deposited on a patterned Si substrate. The trench aspect ratio is 1 : 2 : 5 (bottom width to top width to depth). PbCl$_2$ film was deposited at 85 °C with 600 cycles of 1.5 s Pb(btsa)$_2$ pulse, 0.8 s GaCl$_3$ pulse and 3.0 s purge durations.

2.5 Pb(btsa)$_2$–SnBr$_4$ process

Just like for GaCl$_3$, there were initial challenges in the SnBr$_4$ delivery. When delivered from an open glass boat held at room temperature, SnBr$_4$ sublimed completely during the reactor heating stage prior to the deposition experiment. On the other hand, SnBr$_4$ was insufficiently volatile to be delivered from an external precursor container under its own vapour pressure. For these reasons we resorted to the orifice boats developed for GaCl$_3$. No differences in film properties were observed between films deposited with solid SnBr$_4$ delivered from a boat with a 7 × 5 mm orifice and films deposited with an 80 wt% SnBr$_4$ solution in hexane delivered from a boat with a 1 mm orifice. Based on the lack of differences we chose 7 × 5 mm orifice boats for SnBr$_4$ delivery as their loading was more convenient.

With 0.07 Å per cycle, the Pb(btsa)$_2$–SnBr$_4$ process had the lowest GPC among the processes presented in this work. This GPC decreased further with increasing deposition temperature (Fig. S13c†). At 65 °C the GPC saturated with respect to the SnBr$_4$ pulse duration and was independent of the purge duration but did not saturate with respect to the Pb(btsa)$_2$ pulse duration (Fig. S13d–f†). The film thickness increased linearly with the number of deposition cycles (Fig. S13g†) and the films had a visible thickness gradient (Fig. S13a†).

The films were amorphous at all deposition temperatures with two very wide features (FWHM 8.4° of 2θ) visible in the XRD patterns (Fig. S13i†). FESEM revealed that the films are smooth and lack any features, as expected from amorphous films (Fig. S13b†). The measured refractive index of 1.9 was lower than the literature values (2.4–2.6)[16] reported for PbBr$_2$. Furthermore, the films contained impurities that were mainly Sn, O and H (Fig. S13h†). The Pb to Br ratio, on the other hand, was close to stoichiometric and the observed element concentrations were similar to those in the (Pb(gem))$_2$–SnCl$_4$ process. Following the same reasoning, we speculate that the addressed impurity contents are caused by an incorporation of an air sensitive by-product during the deposition.

To explain the differences between the Pb(btsa)$_2$–SnX$_4$ deposition behaviour (Table 1) we performed a quantum chemical investigation using ORCA 5 and the general-purpose composite density functional theory (DFT) method r^{2}SCAN-3c [47] (Table 2). In general, reactions that produce crystalline PbX$_2$(s) were highly favourable ($\Delta G \leq -110$ kJ mol^{-1}),

Table 2 Free energy changes in kJ mol^{-1} for selected reactions relevant to PbX$_2$ ALD and etching using Pb(btsa)$_2$ and SnX$_4$ under standard conditions

Reaction	Type	X = Cl	Br	I
Pb(btsa)$_2$ + SnX$_4$ → PbX$_2$(s) + Sn(btsa)$_2$X$_2$	Deposition	−228	−213	−192
Pb(btsa)$_2$ + Sn(btsa)X$_3$ → PbX$_2$(s) + Sn(btsa)$_3$X	Deposition	−137	−124	−110
Pb(btsa)$_2$ + SnX$_4$ → Pb(btsa)X + Sn(btsa)X$_3$	Intermediate	−68	−63	−50
Pb(btsa)$_2$ + PbX$_2$(s) → 2Pb(btsa)X	Intermediate	107	95	91
3Pb(btsa)$_2$ + SnX$_4$ → 3Pb(btsa)X + Sn(btsa)$_3$X	Intermediate	−97	−92	−69
Pb(btsa)X + Sn(btsa)$_3$X → Pb(btsa)$_2$ + Sn(btsa)$_2$X$_2$	Etch	−24	−26	−33

including disproportionation of the heteroleptic Pb(btsa)X(g) to Pb(btsa)$_2$(g) and PbX$_2$(s), which supports our observations here and previously[10] that SnX$_4$ can deposit crystalline PbX$_2$.

We then investigated by quantum chemical calculations the reaction that causes etching with SnCl$_4$, but deposition with SnBr$_4$ and SnI$_4$. We speculated that Pb(btsa)$_2$ itself was the only etch product capable of removing Pb(II) ions from the film at such low temperatures, and found that the only favourable reaction resulting in Pb(btsa)$_2$ formation is between Pb(btsa)X(g) and Sn(btsa)$_3$X(g). The free energy change of this reaction is, contrary to the experimental evidence, larger for the iodide than the bromide or chloride, but the difference was too small ($\Delta G \sim 4$ kJ mol^{-1}) to be considered definitive evidence at the chosen level of theory. Besides, the free energy change of the reactions for each halide was small ($-33 < \Delta G < -24$ kJ mol^{-1}). However, the formation of the reactive intermediates Sn(btsa)$_3$X(g) and Pb(btsa)X(g) from 3 eq. of Pb(btsa)$_2$(g) and 1 eq. of SnX$_4$(g) was most favourable for the chloride ($\Delta G = -97$ kJ mol^{-1}), followed closely by the bromide ($\Delta G = -92$ kJ mol^{-1}), while it was far less favourable for the iodide ($\Delta G = -69$ kJ mol^{-1}). As the reason for the etching observed when using SnCl$_4$ and the impurities observed when using SnBr$_4$, we propose a higher volatility of the intermediate heteroleptic Sn(IV) amide chlorides than the analogous bromides. This common trend between analogous group 17 compounds would cause the chlorides to evaporate (*i.e.*, cause etching) while the bromides would not (*i.e.*, incorporate air-sensitive impurities). On the other hand, it seems far less favourable for the heteroleptic intermediates to form for the iodide, which results in ALD of pure PbI$_2$ films from Pb(btsa)$_2$ and SnI$_4$.[10]

2.6 Pb(btsa)$_2$–TiBr$_4$ process

The Pb(btsa)$_2$–TiBr$_4$ process deposits uniform PbBr$_2$ films (Fig. 5a and b inset). The GPC is independent of the deposition temperature in the 65–85 °C range and decreases abruptly when the deposition temperature increases above 85 °C (Fig. 5b). At 75 °C the GPC is independent of the purge durations when they are 0.5 s and longer (Fig. 5c) and saturates with respect to both precursor pulse durations (Fig. 5d and e). The film thickness at 75 °C increases linearly with an increasing number of cycles, apart from an initial steeper slope, that we attribute to enhanced nucleation on Si (Fig. 5f).

XRD and Raman show that the films deposited with the Pb(btsa)$_2$–TiBr$_4$ process were crystalline PbBr$_2$ (Fig. 6a and b). Grain boundaries in the PbBr$_2$ films are not as evident as in the PbCl$_2$ films made with GaCl$_3$ (Fig. 6c, d and Fig. S15†). Upon growth, PbBr$_2$ grains partially coalesce together into clusters that give the films their botryoidal texture. A higher deposition temperature promotes the fusion of grains, causing the films to become smoother (Fig. 6e). At 90 °C the GPC decreases abruptly (Fig. 5b), the films deposited with the same number of cycles become thinner and discontinuous which causes an increase in relative roughness. No deposition occurs at temperatures higher than 105 °C (Fig. 5b and Fig. S15f–h†). An 81 nm thick film deposited at 75 °C, had an 11 nm surface roughness (R_q) which is 13% of the film thickness and is in the range of what we typically observe for crystalline halide films made *via* ALD.[10,11]

ToF-ERDA shows that small amounts of titanium (0.5 at%) are present in the films as well as some lighter elements with oxygen having the highest concentration (Fig. S16†). The same
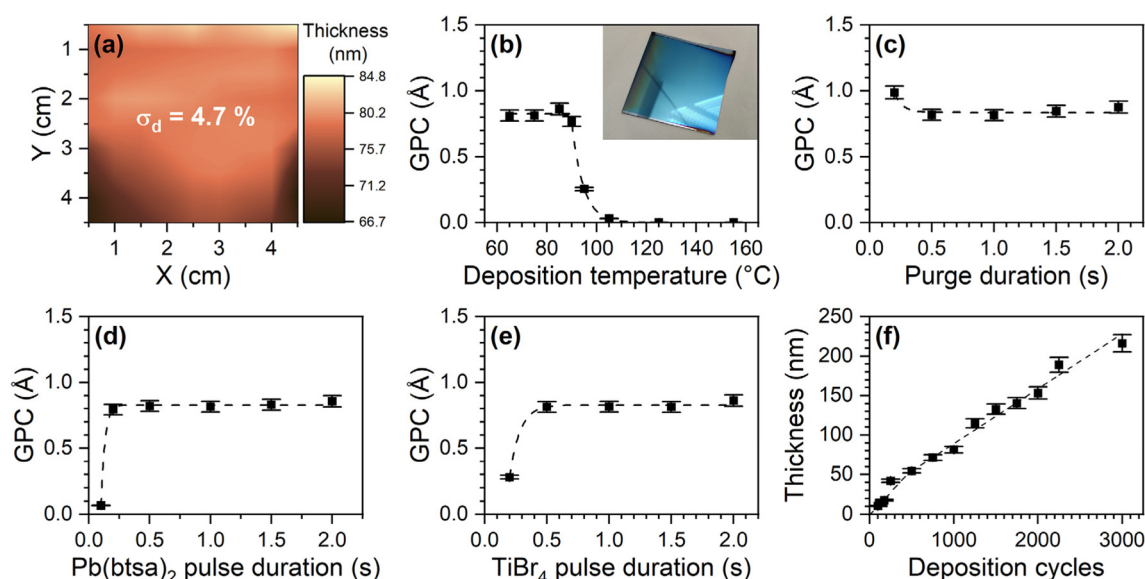
Fig. 5 (a) Ellipsometry thickness maps of a PbBr$_2$ film deposited on 5 × 5 cm Si substrate (0.5 cm edge exclusion). PbBr$_2$ GPC as a function of (b) deposition temperature as well as (c) purge, (d) Pb(btsa)$_2$ pulse and (e) TiBr$_4$ pulse duration. (f) Shows PbBr$_2$ film thickness as a function of deposition cycles. The inset in (b) is a digital photograph of a PbBr$_2$ film. In (c) both purge durations were adjusted in a single deposition experiment. Unless otherwise evident the films were deposited at 75 °C with 1000 cycles. The pulse durations were 1.0 s and 1.5 s long for Pb(btsa)$_2$ and TiBr$_4$ respectively and were separated by 1.0 s long purges. Thicknesses were measured by ellipsometry.

Fig. 6 (a) XRD patterns of PbBr$_2$ films deposited at different temperatures. Enlarged and indexed XRD patterns are shown in Fig. S14.† (b) Raman spectra of PbBr$_2$ film on thermal SiO$_2$/Si substrate and of a tablet pressed from commercial PbBr$_2$ powder (99.998%, Alfa Aesar). The PbBr$_2$ film was deposited with 1600 cycles. Literature patterns for PbBr$_2$ [80] and Si [79] are shown for reference. FESEM image of a PbBr$_2$ film taken (c) top-down and (d) from cross-section. (e) PbBr$_2$ film roughness relative to thickness as a function of deposition temperature. (f) Transmittance of a PbBr$_2$ film deposited on sapphire and of a bare sapphire wafer. Reflectance spectrum is shown in Fig. S19.† Inset shows the Tauc plot constructed from the transmittance spectrum of the PbBr$_2$ film in (f). Unless otherwise evident the depositions were made at 75 °C, with 1000 cycles of 1.0 s Pb(btsa)$_2$ pulse, 1.5 s TiBr$_4$ pulse and 1.0 s purge durations.

elements are also visible in the XPS spectra (Fig. S17a†). Like the Pb 4f spectra of the PbCl$_2$ film, the Pb 4f spectrum of the PbBr$_2$ film consists of two doublets (Fig. S17b†). The higher intensity doublet (139.1 and 144 eV) corresponds to PbBr$_2$ [48] and the lower intensity one (136.9 and 141.8 eV) to Pb^0.[32] The Br 3d spectrum features a single doublet corresponding to PbBr$_2$.[48] Titanium Ti 2p spectrum is also a single doublet that fits TiO$_2$ (Fig. S17d†).[49] A component corresponding to the oxygen in the TiO$_2$ is also present in the O 1s spectrum (530.6 eV, Fig. S17e†).[49] Otherwise, the O 1s spectrum of the PbBr$_2$ film (Fig. S17e†) is comprised of similar oxygen containing surface contaminants as in the case of PbCl$_2$ (Fig. S10e†).[42] Since the deposition process is oxygen free, the oxygen content most likely originates from the exposure of the PbBr$_2$ film to air. In case of PbBr$_2$ films, XRD shows that lead oxybromide hydrate starts to form upon prolonged exposure to air (Fig. S18†).

The optical properties of the PbBr$_2$ films correspond to those reported for PbBr$_2$ in literature. The refractive index is 2.5 (lit. 2.4–2.6)[16] and the band gap extracted from the Tauc plot, that was constructed from the transmittance data (Fig. 6g), is 3.7 eV (lit. 3.8–4.2 eV[43–46,50]). A comparison of film compositions and refractive indices across the studied processes (Table 1) suggests that a significant impurity content causes a significant deviation of the observed refractive index from that of the bulk compound. Mind, that a small decrease in the refractive index relative to the bulk value is common for thin film samples.[51,52]

Just like PbCl$_2$ deposited with GaCl$_3$, PbBr$_2$ deposited with TiBr$_4$ grew conformally on a patterned Si substrate with no need for any additional optimization of process parameters (Fig. 8). Due to the crystallite texture that the PbBr$_2$ process yields, the PbBr$_2$ film is rougher than the PbCl$_2$ film (Fig. 4).

We constructed simple UV photodetectors (photoresistors, Fig. 7a–c) to test whether Pb(btsa)$_2$–GaCl$_3$ and Pb(btsa)$_2$–TiBr$_4$ processes deposit films of sufficient quality for optoelectronic devices. As expected for the wide band-gap materials, the dark current was small (10^{-11} A) and under UV illumination the current increased several orders of magnitude (Fig. 7d). The PbCl$_2$ based photodetector exhibited a larger increase in current under the UV illumination compared to the PbBr$_2$ based device. These simple devices show that the halide films can be used in optoelectronic devices.

2.7 Mixed lead halides

PbCl$_2$ and PbBr$_2$ are isostructural with the cotunnite structure (Fig. S20a and b†)[53] whereas PbI$_2$ has a 2D structure with a large number of polytypes that differ from each other in how the 2D layers stack on top of each other (Fig. S20c and d†).[54] Each pair of the binary lead halide compounds can form a ternary compound: PbBrCl, PbICl and PbBrI. Also, the ternary compounds adopt the cotunnite structure (Fig. S20e–g†).

We used the supercycle approach to test whether the binary halide processes are compatible with each other and whether
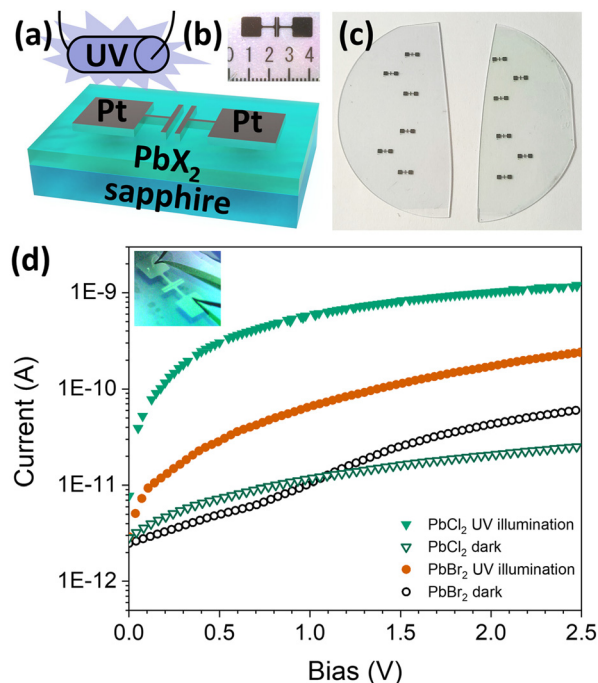
Fig. 7 (a) Schematic structure and (b) photograph of the sapphire/lead halide/Pt photodetector structure. Millimetre ruler is shown for reference. (c) Photograph of the $PbCl_2$ based (left) and $PbBr_2$ based (right) device structures. (d) $I–V$ curves of a $PbCl_2$ and $PbBr_2$ devices from (c) in dark and under UV illumination. Inset photograph shows a $PbBr_2$ based device with needle probe contacts under UV illumination. The $PbCl_2$ film was deposited at 85 °C with 600 cycles consisting of 1.5 s $Pb(btsa)_2$ pulse, 0.8 s $GaCl_3$ pulse and 3.0 s purge durations. The $PbBr_2$ film was deposited at 75 °C with 2900 cycles consisting of 1.0 s $Pb(btsa)_2$ pulse, 1.5 s $TiBr_4$ pulse and 1.0 s purge durations.
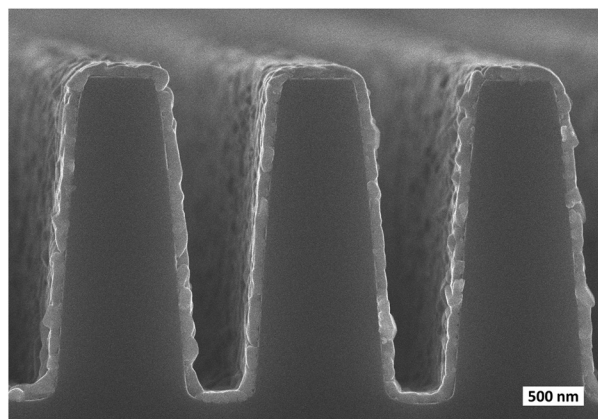

Fig. 8 FESEM image of a $PbBr_2$ film deposited on a patterned Si substrate. The trench aspect ratio is 1 : 2 : 5 (bottom width to top width to depth). $PbBr_2$ film was deposited at 75 °C with 1000 cycles of 1.0 s $Pb(btsa)_2$ pulse, 1.5 s $TiBr_4$ pulse and 1.0 s purge durations.

mixed lead halides can be deposited. The processes that we chose were $Pb(btsa)_2$–$GaCl_3$ for $PbCl_2$, $Pb(btsa)_2$–$TiBr_4$ for $PbBr_2$ and $Pb(btsa)_2$–SnI_4 for PbI_2.[10] The deposition experiments consisted of 50 supercycles which in turn consisted of 20 binary process cycles of two lead halides yielding a total of
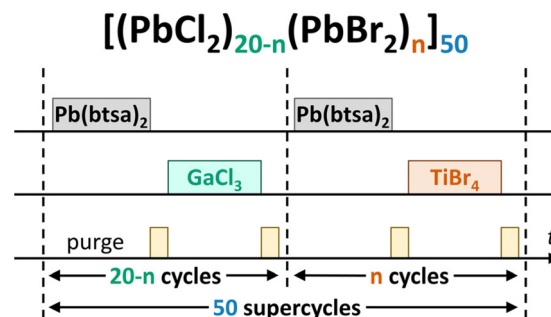

Fig. 9 Scheme of a pulse sequence used to deposit mixed lead halides. $PbCl_2$ and $PbBr_2$ binary processes are used as an example. The total number of deposition cycles was always 1000, as $n \leq 20$.

1000 deposition cycles (Fig. 9). We varied the ratio between the binary lead halide process cycles and studied how that affected the element concentrations, phase composition and optical properties of the films.

Composition of the mixed lead halide films does not have a linear dependence on the ratio of the binary lead halide processes. This lack of the linear dependence is common for the supercycle approach.[55–58] In the $PbCl_2$–$PbBr_2$ and $PbBr_2$–PbI_2 systems, the composition is shifted heavily in favour of the heavier halide (Fig. 10a and g). Only a couple of cycles of the heavier halide in the supercycle cause a significant composition deviation. The effect is stronger in the $PbCl_2$–$PbBr_2$ system. On the other hand, in the $PbCl_2$–PbI_2 system the deviation in the halide content from the ratio of the binary process cycles is more gradual with a plateau at around 1 : 1 halide ratio for the intermediate cycle ratios (Fig. 10d). In the supercycle approach a difference in GPCs of the binary processes can cause nonlinear dependence of the composition on the ratio of binary process cycles. In our case, however, the GPC trend is reverse with $PbCl_2$ having the highest GPC and PbI_2 the lowest. Another possible explanation is that in mixed halide processes a halide exchange reaction occurs, followed by distribution of the heavier halide in the film *via* diffusion.

The $PbCl_2$–$PbBr_2$ system is a solid solution. At all the examined cycle ratios, the films are phase pure $PbBr_xCl_{2-x}$ (Fig. 10b and Fig. S21a†). Mixed halide cotunnites also form in the $PbCl_2$–PbI_2 and $PbBr_2$–PbI_2 systems but minor reflections of one or both binary phases are always present in the XRD patterns of the films (Fig. 10e, h and Fig. S21b, c†). The films look homogenous when examined with SEM (Fig. S22†). This, however, does not contradict the presence of the binary phases as they can segregate at the grain boundaries instead of forming separate macro-scaled domains.

In all the systems changes in the optical properties of the films follow changes in the composition of the films (Fig. 10c, f and i). The bandgap of the films can be tuned in a range from 2.4 to 4.9 eV.

The $Pb(btsa)_2$–$GaCl_3$, –$TiBr_4$ and –SnI_4 processes are compatible with each other. We saw no signs of undesirable side reactions or phases. However, there is room for further optimization of the supercycle's parameters. Given the non-
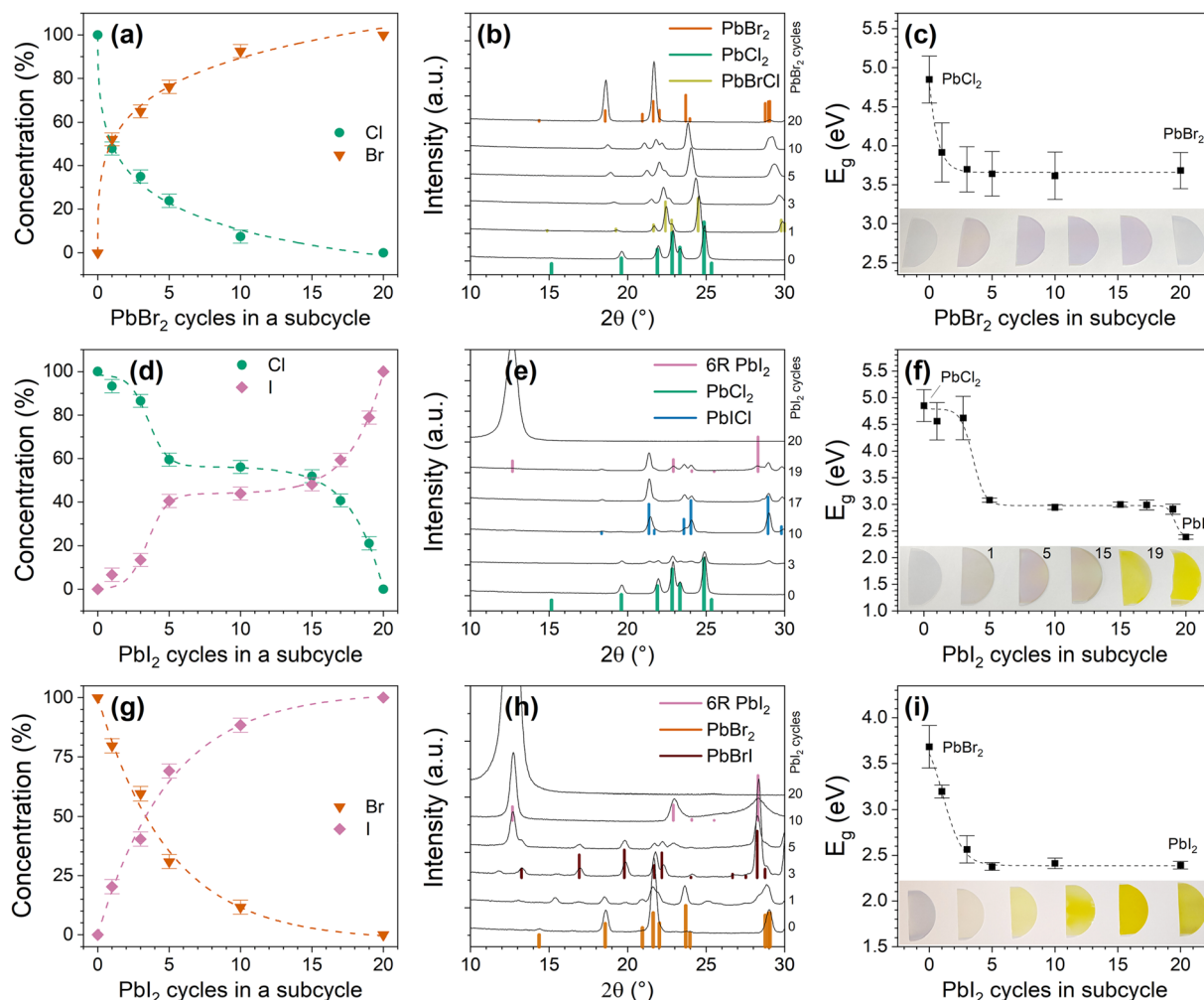
Fig. 10 (a) Halide concentration, (b) XRD patterns and (c) bandgaps of $PbBr_xCl_{2-x}$ films. (d–f) and (g–i) Show same sets of data for PbI_xCl_{2-x} and $PbBr_xI_{2-x}$ respectively. Insets show digital photographs of mixed halide films deposited on sapphire that were used for transmittance measurements. Bandgaps were extracted from Tauc plots constructed from this transmittance data. Halide concentrations are obtained from EDS measurements and normalized to the total halide content. Relevant XRD reference patterns, including $PbBr_2$ (ICDD 31-679), $PbCl_2$ (ICDD 26-1150), PbBrCl (ICDD 24-1088), 6R PbI_2 (COD 9009142), PbICl (ICDD 43-949) and PbBrI (ICSD 22138) are shown. All films were deposited at 75 °C. XRD patterns in a wider 2θ range are shown in Fig. S21.†

linear dependence of the composition on the cycle ratios in all the three systems, an increase in the total number of binary process cycles that comprise the supercycle will enable finer composition tunability on the lighter halide end.

3. Conclusions

We showed that $PbCl_2$ and $PbBr_2$ can be deposited with ALD at low temperatures (≤100 °C). The $Pb(btsa)_2$–$GaCl_3$ and the $Pb(btsa)_2$–$TiBr_4$ processes produce the films with the best properties. These processes deposit pure, crystalline, uniform and conformal films. All other processes that we studied namely $Pb(btsa)_2$–$SnCl_4$, $Pb(btsa)_2$–$SnBr_4$, $Pb(btsa)_2$–$TiCl_4$ and $(Pb(gem))_2$–$SnCl_4$ were found to be unideal as ALD processes. The observed issues showcase how subtle differences in the halide precursors have major impact on the behaviour of by-products

and ultimately on the film properties. This, in turn, highlights the importance of empirical and computational mechanism studies for further development of metal halide ALD processes.

Furthermore, we showed that mixed lead halide films can be deposited with ALD. $Pb(btsa)_2$–$GaCl_3$ and –$TiBr_4$ processes are compatible with each other as well as with the earlier reported $Pb(btsa)_2$–SnI_4 process for PbI_2. One plausible direction for future research efforts is further optimization of the mixed lead halide process parameters and their conversion to halide perovskites.

4. Experimental

4.1 Precursors

$Pb(btsa)_2$ was synthesized from $PbCl_2$ (99.999%, Alfa Aesar) and Li(btsa) (97%, Sigma Aldrich) using Schlenk line tech-

niques. The synthesis procedure is based on the work of Gynane *et al.*[59] Li(btsa) dissolved in *n*-hexane was added dropwise to $PbCl_2$ in THF over a cold water bath. The bottle was wrapped in an aluminium foil to protect the mixture from light and left to stir overnight. THF was removed *in vacuo* and replaced with *n*-hexane. The mixture was filtered through a glass filter frit with Celite yielding a clear canary yellow solution. Removal of hexane *in vacuo* affords a red orange $Pb(btsa)_2$ oily liquid. The liquid can be used as is, but it slowly decomposes during storage inside glove box despite protection from light. Decomposition is visible by the darkening colour of the liquid with time. $Pb(btsa)_2$ is reported to be solid at room temperature.[23,59] Distillation of the liquid $Pb(btsa)_2$ still yielded a liquid. Cooling the distillate with liquid N_2 caused it to solidify into a bright yellow solid. The solid does not melt upon warming back to room temperature and is stable upon storage. Solid ^{1}H NMR (400.144 MHz, 298 K, C_6D_6): δ 0.25 (s, 36 H). ^{13}C NMR (100.616 MHz, 298 K, C_6D_6): δ 5.93. In film depositions there were no differences regardless of whether liquid or solid $Pb(btsa)_2$ was used. Literature provides more data on the sensitivity and stability of $Pb(btsa)_2$.[21,23,59]

Bis[lead(II) *N,N′*-di-*tert*-butyl-1,1-dimethylsilanediamide] (Pb (gem))$_2$ was prepared following a literature procedure.[60] Dilithio diamide $Me_2Si[N(Li)^tBu]_2$ (1 eq., 7.928 g, 37.00 mmol), recrystallized from hexane, and a slight excess of $PbCl_2$ (1.1 eq., 11.31 g, 40.70 mmol) were placed in a 250 mL round-bottom flask with a magnetic stir-bar in a N_2-filled dry-box. Then, 100 mL of Et_2O was added all at once and the flask was closed with a greased glass stopper held shut with a plastic Keck clip. A slight exotherm occurs as the dilithio salt dissolves and begins to react with $PbCl_2$. The reaction mixture was then stirred overnight (*ca.* 16 h). After the reaction had proceeded, an off-white precipitate developed under a bright orange supernatant liquid which was separated by filtration through a pad of Celite and a medium porosity sintered glass filter to yield a bright orange filtrate. (Note: If crude or *in situ* generated $Me_2Si[N(Li)^tBu]_2$ is used, a dark precipitate, presumably contaminated with Pb(0), may be obtained with a slightly diminished yield.) Solvent and other volatiles were removed under vacuum, and a crude orange solid was obtained. The crude product was then purified directly by vacuum sublimation (100 °C/40 mTorr) into an air-cooled 90° glass elbow to yield (Pb(gem))$_2$ as yellow thermochromic crystals that turn orange upon heating and red upon melting (14.04 g, 92% yield based on ligand). M.p. 85 °C, sublimed; lit. 85 °C, recrys. Et_2O. Crystals suitable for X-ray diffraction were grown by slowly cooling a solution of (Pb(gem))$_2$ in toluene overnight at −49 °C. ^{1}H NMR (300 MHz, C_6D_6, $\delta_{C_6D_5H}$ = 7.16 ppm): 0.42 (6H, s, Si(CH_3)$_2$), 1.24 (18H, s, PbN–C(CH_3)$_3$). More data on the sensitivity and stability of (Pb(gem))$_2$ can be found in literature.[21]

Crystals were attached to the tip of an appropriately sized MiTeGen mount with Paratone-N oil. Measurements were made on a Bruker APEXII CCD equipped diffractometer using monochromated Mo Kα radiation (λ = 0.71073 Å; 30 mA, 50 mV) at 125 K. APEX3 software[61] was used for the initial orientation and unit cell were indexed using a least-squares

analysis of a random set of reflections collected from three series of 0.5° wide scans, 10 seconds per frame and 12 frames per series that were well distributed in reciprocal space. For data collection, four ω-scan frame series were collected with 0.5° wide scans, 5 seconds frames and 366 frames per series at varying φ angles (φ = 0°, 90°, 180°, 270°). The crystal to detector distance was set to 6 cm and a complete sphere of data was collected. Cell refinement and data reduction were performed with the Bruker APEX3 software, which corrects for beam inhomogeneity, possible crystal decay, Lorentz and polarization effects. Data processing and a multi-scan absorption correction was applied using APEX3 software package. The structure was solved using the SHELXT[62] using Intrinsic phasing and all non-hydrogen atoms were refined anisotropically with the SHELXL[63] using a combination of the ShelXle graphical user interface[64] and OLEX2.[65]

Commercial halides: $SnCl_4$ (98%, STREM), $SnBr_4$ (99%, Sigma Aldrich), SnI_4 (99+%, 10 mesh, Thermo Scientific Acros) and $TiCl_4$ (99.9%, Sigma Aldrich) were used as received. $TiBr_4$ (98%, Sigma Aldrich) was ground from as received cm sized chunks to mm sized grains. $GaCl_3$ (ABCR, 99.999%) was dissolved in *n*-hexane (25 wt%). SnI_4, $SnBr_4$, $TiBr_4$ and $GaCl_3$ were stored and handled in glove box. Note that $TiBr_4$ and $GaCl_3$ readily evaporate out of their containers once opened and $TiBr_4$ vapour stains solid objects in contact with it. We recommend storing an opened container inside a second larger container, as neither wax film nor electrical tape can entirely prevent this issue.

4.2 Film deposition

Deposition experiments were performed using a commercial, hot-wall, flow type F120 ALD reactor (ASM Microchemistry Ltd). The pressure in the deposition chamber was *ca.* 10 mbar. Nitrogen (AGA, 99.999%) at a flow rate of 400 sccm was introduced into the reactor through a gas purifier (SAES Pure Gas, MC1-902F, H_2O, O_2, CO, CO_2, H_2, NMHC removal <1 ppb) and acted as carrier and purge gas. $SnCl_4$ and $TiCl_4$ were delivered from external containers where they were held at room temperature. Their delivery lines were equipped with bellows-sealed metering valves (C_v 0.019, Swagelok) that were used to control the dose of the precursor pulsed with solenoid valves. The metering valve was opened for $\frac{1}{2}$ turn for $SnCl_4$ and $TiCl_4$. Pb (btsa)$_2$, SnI_4 and $TiBr_4$ were sublimed from open glass boats held at 60, 65 and 25 °C respectively and pulsed with inert gas valving. $SnBr_4$ was sublimed from closed glass boats with 7 × 5 mm orifice at 25 °C. $GaCl_3$ solution in hexane was sublimed from closed glass boats with a 1 mm orifice at 25 °C. When the reactor is evacuated, hexane evaporates leaving the solid $GaCl_3$ inside closed glass boats (Video S1†).

Most of the depositions were done on 5 × 5 cm native oxide covered silicon substrates (Okmetic). 6″ Si wafers were cut into 5 × 5 cm square pieces which were sonicated thrice: first at 50 °C for 20 min in deionized water (DI) with 20 ml detergent (Branson Industrial Strength Cleaner Concentrate), next at RT for 10 min in DI and finally at RT for 10 min in isopropanol. Clean Si was dried in a heating cabinet at 100 °C for 20 min

and prior to loading into the ALD reactor, blown with N_2 to remove dust. Si substrates with thermal SiO_2 were prepared similarly. Some depositions were made on sapphire wafers (2″, University Wafer). Prior to usage the sapphire wafers were heated at 1000 °C in an air oven for 2 h to induce atomic step formation.[66,67]

Most of the deposited films were stored in a desiccator. Films used for composition analysis were stored in a glove box. However, sample preparation and transfer between storage locations took place in ambient air.

4.3 Film characterization

Film thicknesses were measured either with ellipsometry or with energy dispersive X-ray spectroscopy (EDS). Ellipsometry measurements were made with a Film Sense FS-1 multi-wavelength ellipsometer. Ellipsometry data was fitted with the Cauchy model, which also modelled refractive index values. The reported refractive indices are those for a wavelength of 580 nm. The errors in ellipsometry thickness values were estimated from the fit difference values. EDS was used instead of ellipsometry for processes where the ellipsometry data fit was poor due to roughness, ambiguous composition, or a thickness gradient.

EDS measurements were performed with an Oxford INCA 350 energy spectrometer connected to a Hitachi S-4800 field emission scanning electron microscope (FESEM). Thicknesses were calculated from the EDS data (k ratios) using the GMRFilm software[68] and bulk densities (5.85 and 6.66 g cm^{-3} for $PbCl_2$ and $PbBr_2$ respectively). The errors in EDS thickness values were estimated from weight% uncertainty values of EDS data.

A Hitachi S-4800 field emission scanning electron microscope (FESEM) and a Veeco Multimode V instrument (atomic force microscopy, AFM) were used to study film morphology. AFM tapping mode images were captured in air using two types of silicon probes: NFESP (discontinued) and RFESP-75, both from Bruker. Both probes had a spring constant of 3 N m^{-1} and nominal tip radius of 10 nm. AFM images were flattened to remove artefacts caused by sample tilt and scanner bow. Roughness was calculated as a root-mean-square value (R_q) from flattened images.

X-ray diffraction (XRD) patterns were measured in grazing incidence (GI) geometry with an incident angle of 1°. Most measurements were made on a Rigaku Smartlab diffractometer with Cu Kα-radiation. The measurements regarding the $Pb(btsa)_2$–$SnBr_4$ process and stability tests as well as those of the mixed lead halide films were made with a PANalytical X'pert Pro MPD diffractometer also with Cu Kα-radiation.

The samples used for Raman measurements were deposited on Si wafers with a 320 nm layer of thermal SiO_2. The thickness of the measured film was optimized to achieve amplification in the Raman signal through the interference effect.[69,70] To measure the micro-Raman spectra in a backscattering geometry, a confocal Raman microscope (NT-MDT Ntegra), equipped with a 633 nm laser and a 100× objective, was used. The incident power was 4.5 mW and the spectra were measured with 10 exposures that were 9 s long for $PbCl_2$ and 20 s long for $PbBr_2$.

The elemental compositions of the films were assessed with time-of-flight elastic recoil detection analysis (ToF-ERDA) using a 5 MV tandem accelerator at the accelerator laboratory of the University of Helsinki. The measurements were made with a 40 MeV $^{127}I^{8+}$ beam. The incident beam angle and the detector angle relative to the sample surface was 20°.

Transmittance and reflectance in a wavelength range of 190–1100 nm was measured with a Hitachi U2000 spectrophotometer. An evaporated aluminium mirror served as a reference for the reflectance measurements. Optical band gap values were extracted from Tauc plots constructed from the transmittance data. The band gaps of $PbCl_2$ and $PbBr_2$ were assumed to be direct and allowed.

The XPS measurements were made with a Prevac system featuring an EA-15 hemispherical electrostatic energy analyser and RMC50 monochromatic X-ray source with an Al Kα anode (1486.7 eV). The measurements were conducted under ultra-high vacuum (10^{-10} mbar) and without sputtering. The survey spectra were taken with 200 eV pass energy and slit S 2.5 × 25. The individual spectra were measured with 100 eV pass energy and slit C 0.8 × 25. Metallic lead (99.999%, BDH) was measured and as the reference point the position of the Pb $4f_{7/2}$ in metal state (136.9 eV) was used for these data. Casa XPS software was used to analyse the XPS data. The Tougaard background and LA line shape were used to fit the spectra.

4.4 Photodetector structures

Photodetector structures were made by evaporating platinum electrodes (40 nm) through an Ossila E421 source–drain shadow masks (channel length 30 μm and width 1 mm) onto the lead halide films deposited on sapphire wafers. Needle probes were used to contact the Pt contact pads. The electrical measurements were performed using a Keithley 2450 Source Meter. An in-house mercury vapor discharge lamp was used for UV illumination. The lamp emits primarily at 184 nm (6.7 eV) and 254 nm (4.9 eV).

4.5 Quantum chemical calculations

All calculations were carried out with ORCA 5.0.2[71] using default settings (*i.e.*, grid sizes, convergence criteria, *etc*.). Initial guess geometries were drawn by hand in Avogadro 1.2.0.[72] Geometry optimizations and analytic frequency calculations were then performed with the composite density functional theory (DFT) method r^{2}SCAN-3c,[47] which combines the r^{2}SCAN meta-generalized gradient approximation (mGGA) exchange–correlation functional,[73] refitted charge-dependent D4 London dispersion correction,[73–75] geometric counter-poise (gCP) basis set superposition error (BSSE) correction,[73,76] and the def2-mTZVPP atomic orbital basis set. Stationary points were confirmed to have all real frequencies, and all thermodynamic quantities were calculated using default settings under standard conditions in the gas phase. For reactions producing crystalline $PbX_2(s)$, the known sublimation free energies under standard conditions (HSC Chemistry 5.11,

Outokumpu Research Oy) were included to better model the solid–gas surface chemistry. Illustrations of the calculated geometries were rendered procedurally with Jmol[77] and may be found in the ESI† along with electronic energies and thermodynamic corrections of relevant molecular species (Tables S1–S3†).

Author contributions

Conflicts of interest

There are no conflicts to declare.

Acknowledgements

References

1 W. A. Dunlap-Shohl, Y. Zhou, N. P. Padture and D. B. Mitzi, Synthetic Approaches for Halide Perovskite Thin Films, *Chem. Rev.*, 2019, **119**, 3193–3295.

2 A. K. Jena, A. Kulkarni and T. Miyasaka, Halide Perovskite Photovoltaics: Background, Status, and Future Prospects, *Chem. Rev.*, 2019, **119**, 3036–3103.

3 L. Chouhan, S. Ghimire, C. Subrahmanyam, T. Miyasaka and V. Biju, Synthesis, optoelectronic properties and applications of halide perovskites, *Chem. Soc. Rev.*, 2020, **49**, 2869–2885.

4 H. Kim, J. S. Han, J. Choi, S. Y. Kim and H. W. Jang, Halide Perovskites for Applications beyond Photovoltaics, *Small Methods*, 2018, **2**, 1700310.

5 B. Jeong, H. Han and C. Park, Micro- and Nanopatterning of Halide Perovskites Where Crystal Engineering for Emerging Photoelectronics Meets Integrated Device Array Technology, *Adv. Mater.*, 2020, **32**, 2000597.

6 X.-K. Liu, W. Xu, S. Bai, Y. Jin, J. Wang, R. H. Friend and F. Gao, Metal halide perovskites for light-emitting diodes, *Nat. Mater.*, 2021, **20**, 10–21.

7 Y. Zhou, J. Chen, O. M. Bakr and O. F. Mohammed, Metal Halide Perovskites for X-ray Imaging Scintillators and Detectors, *ACS Energy Lett.*, 2021, **6**, 739–768.

8 F. Li, W. Yu, X. Guan and T. Wu, Emerging Transistor Applications Enabled by Halide Perovskites, *Acc. Mater. Res.*, 2022, **3**, 8–20.

9 J. R. Ommen, A. Goulas and R. L. Puurunen, *Kirk–Othmer Encyclopedia of Chemical Technology*, Wiley, 2021, pp. 1–42.

10 G. Popov, M. Mattinen, T. Hatanpää, M. Vehkamäki, M. Kemell, K. Mizohata, J. Räisänen, M. Ritala and M. Leskelä, Atomic Layer Deposition of PbI_2 Thin Films, *Chem. Mater.*, 2019, **31**, 1101–1109.

11 A. Weiß, G. Popov, E. Atosuo, A. Vihervaara, P. Jalkanen, M. Vehkamäki, M. Leskelä, M. Ritala and M. Kemell, Atomic Layer Deposition of CsI and $CsPbI_3$, *Chem. Mater.*, 2022, **34**, 6087–6097.

12 T. Matsui, T. Yamamoto, T. Nishihara, R. Morisawa, T. Yokoyama, T. Sekiguchi and T. Negami, Compositional Engineering for Thermally Stable, Highly Efficient Perovskite Solar Cells Exceeding 20% Power Conversion Efficiency with 85 °C/85% 1000 h Stability, *Adv. Mater.*, 2019, **31**, 1806823.

13 G. Natarajan, P. S. Maydannik, D. C. Cameron, I. Akopyan and B. V. Novikov, Atomic layer deposition of CuCl nanoparticles, *Appl. Phys. Lett.*, 2010, **97**, 241905.

14 J. N. Vagott, K. Bairley, J. Hidalgo, C. A. R. Perini, A.-F. Castro-Méndez, S. Lombardo, B. Lai, L. Zhang, K. Kisslinger, J. Kacher and J.-P. Correa-Baena, PbI_2 Nanocrystal Growth by Atomic Layer Deposition from Pb (tmhd)$_2$ and HI, *Chem. Mater.*, 2022, **34**, 2553–2561.

15 Database of ALD processes, **https://www.atomiclimits.com/alddatabase/**, accessed Feb 15, 2022, DOI: **10.6100/alddatabase**.

16 S. S. Batsanov, E. D. Ruchkin and I. A. Poroshina, *Refractive Indices of Solids*, Springer Singapore, Singapore, 2016.

17 H. A. Evans, Y. Wu, R. Seshadri and A. K. Cheetham, Perovskite-related ReO_3-type structures, *Nat. Rev. Mater.*, 2020, **5**, 196–213.

18 H. P. Beck and F. Kühn, Studies on ABX_6 Compounds. III. The $SnZrCl_6$ structure type, *Z. Anorg. Allg. Chem.*, 1995, **621**, 1655–1658.

19 S. I. Troyanov, B. I. Kharisov and S. S. Berdonosov, Crystal structure of $FeZrCl_6$ – a new structural type for ABX_6 compounds (Russian), *Zh. Neorg. Khim.*, 1992, **37**, 2424–2429.

20 S. S. Berdonosov, B. I. Kharisov, V. Y. Lebedev and I. V. Melikhov, Synthesis and Properties of Iron(II)

Hexachlorohafnate (Russian), *Zh. Neorg. Khim.*, 1993, **38**, 476–477.

21 G. Bacic, *PhD thesis*, Carleton University, 2021.

22 B. Wrackmeyer, A. Pedall and J. Weidinger, N-Silylaminotin Trichlorides. Synthesis and Characterisation by Multinuclear Magnetic Resonance Spectroscopy, *Z. Naturforsch. B*, 2001, **56**, 1009–1014.

23 G. Bačić, D. Zanders, B. Mallick, A. Devi and S. T. Barry, Designing Stability into Thermally Reactive Plumbylenes, *Inorg. Chem.*, 2018, **57**, 8218–8226.

24 O. H. Kim, D. Kim and T. Anderson, Atomic layer deposition of GaN using $GaCl_3$ and NH_3, *J. Vac. Sci. Technol., A*, 2009, **27**, 923–928.

25 T. Sarnet, T. Hatanpää, M. Laitinen, T. Sajavaara, K. Mizohata, M. Ritala and M. Leskelä, Alkylsilyl compounds as enablers of atomic layer deposition: analysis of $(Et_3Si)_3As$ through the GaAs process, *J. Mater. Chem. C*, 2016, **4**, 449–454.

26 Y. Jin, R. Kobayashi, K. Fujii and F. Hasegawa, Atomic Layer Epitaxy of GaAs Using $GaCl_3$ and AsH_3, *Jpn. J. Appl. Phys.*, 1990, **29**, L1350–L1352.

27 H. Bürger, J. Cichon, U. Goetze, U. Wannagat and H. J. Wismar, Beiträgezur chemie der silicium-stickstoff-verbindungen, *J. Organomet. Chem.*, 1971, **33**, 1–12.

28 D. A. Atwood, V. O. Atwood, A. H. Cowley, R. A. Jones, J. L. Atwood and S. G. Bott, Synthesis and Structural Characterization of Homoleptic Gallium Amides, *Inorg. Chem.*, 1994, **33**, 3251–3254.

29 E. A. Mazurenko, L. I. Tsymbal and L. I. Zheleznova, Investigation of the thermal properties of tris-bis(trimethyl-silyl)amides of Al, Ga, In and their derivatives, *Ukr. Chem. J.*, 2000, **66**, 59–61.

30 E. A. Mazurenko, L. I. Tsymbal and L. I. Zheleznova, Synthesis of aluminium, gallium and indium hexamethyi disilazanates, *Ukr. Chem. J.*, 2000, **66**, 13–17.

31 J. Yu, X. Zhang, B. Jin, J. Chen, Y. Huang and Z. Wang, Silica aluminum xerogel-based sorbent for removal of vola-tilized $PbCl_2$ during the incineration: Improvement on mass-transfer limitations via high porosity, *Sci. Total Environ.*, 2021, **782**, 146925.

32 J. A. Taylor and D. L. Perry, An X-ray photoelectron and electron energy loss study of the oxidation of lead, *J. Vac. Sci. Technol., A*, 1984, **2**, 771–774.

33 D. Wei, F. Ma, R. Wang, S. Dou, P. Cui, H. Huang, J. Ji, E. Jia, X. Jia, S. Sajid, A. M. Elseman, L. Chu, Y. Li, B. Jiang, J. Qiao, Y. Yuan and M. Li, Ion-Migration Inhibition by the Cation–π Interaction in Perovskite Materials for Efficient and Stable Perovskite Solar Cells, *Adv. Mater.*, 2018, **30**, 1–10.

34 W. Zhang, S. Pathak, N. Sakai, T. Stergiopoulos, P. K. Nayak, N. K. Noel, A. A. Haghighirad, V. M. Burlakov, D. W. Dequilettes, A. Sadhanala, W. Li, L. Wang, D. S. Ginger, R. H. Friend and H. J. Snaith, Enhanced opto-electronic quality of perovskite thin films with hypopho-sphorous acid for planar heterojunction solar cells, *Nat. Commun.*, 2015, **6**(1), 10030.

35 T. Wu, Y. Wang, X. Li, Y. Wu, X. Meng, D. Cui, X. Yang and L. Han, Efficient Defect Passivation for Perovskite Solar Cells by Controlling the Electron Density Distribution of Donor-π-Acceptor Molecules, *Adv. Energy Mater.*, 2019, **9**, 1–8.

36 J. Chun-Ren Ke, A. S. Walton, D. J. Lewis, A. Tedstone, P. O'Brien, A. G. Thomas and W. R. Flavell, In situ investi-gation of degradation at organometal halide perovskite sur-faces by X-ray photoelectron spectroscopy at realistic water vapour pressure, *Chem. Commun.*, 2017, **53**, 5231–5234.

37 C. Dokkhan, M. Z. Mokhtar, C.-R. Ke, A. S. Walton, Q. Chen, N. W. Hodson, Q. Lian and B. R. Saunders, Modulating Crystallization in Semitransparent Perovskite Films Using Submicrometer Spongelike Polymer Colloid Particles to Improve Solar Cell Performance, *ACS Appl. Energy Mater.*, 2019, **2**, 6624–6633.

38 T.-W. Ng, C.-Y. Chan, M.-F. Lo, Z. Q. Guan and C.-S. Lee, Formation chemistry of perovskites with mixed iodide/ chloride content and the implications on charge transport properties, *J. Mater. Chem. A*, 2015, **3**, 9081–9085.

39 R. K. Ramachandran, J. Dendooven, J. Botterman, S. Pulinthanathu Sree, D. Poelman, J. A. Martens, H. Poelman and C. Detavernier, Plasma enhanced atomic layer deposition of Ga_2O_3 thin films, *J. Mater. Chem. A*, 2014, **2**, 19232–19238.

40 M. K. Yadav, A. Mondal, S. Das, S. K. Sharma and A. Bag, Impact of annealing temperature on band-alignment of PLD grown $Ga_2O_3/Si(100)$ heterointerface, *J. Alloys Compd.*, 2020, **819**, 153052.

41 A. N. Zelikman, O. E. Kreĭn and G. V. Samsonov, in *Metallurgy of rare metals (Metallurgiva redkikh metallov)*, ed. L. V. Belyaevskaya, Israel Program for Scientific Translations; available from the U.S. Dept. of Commerce Clearinghouse for Federal Scientific and Technical Information, Springfield, Virginia, 2nd edn, 1966, p. 338.

42 E. McCafferty and J. P. Wightman, Determination of the concentration of surface hydroxyl groups on metal oxide films by a quantitative XPS method, *Surf. Interface Anal.*, 1998, **26**, 549–564.

43 V. G. Plekhanov, Investigation of the reflectance spectra of $PbCl_2$ and $PbBr_2$ single crystals with orthorhombic struc-ture, *Phys. Status Solidi*, 1975, **68**, K35–K38.

44 M. Fujita, M. Itoh and Y. Bokumoto, Optical spectra and electronic structures of lead halides, *Phys. Rev. B: Condens. Matter Mater. Phys.*, 2000, **61**, 15731–15737.

45 V. Plekhanov, Optical constants of lead halides, *Phys. Status Solidi B*, 1973, **57**, K55–K59.

46 R. Kink, T. Avarmaa, V. Kisand, A. Löhmus, I. Kink and I. Martinson, Luminescence of cation excitons in $PbCl_2$ and $PbBr_2$ crystals in a wide excitation VUV region, *J. Phys.: Condens. Matter*, 1998, **10**, 693–700.

47 S. Grimme, A. Hansen, S. Ehlert and J.-M. Mewes, r^2SCAN-3c: A "Swiss army knife" composite electronic-structure method, *J. Chem. Phys.*, 2021, **154**, 064103.

48 L. Yuan, R. Patterson, W. Cao, Z. Zhang, Z. Zhang, J. A. Stride, P. Reece, G. Conibeer and S. Huang, Air-

stable PbS quantum dots synthesized with slow reaction kinetics via a PbBr$_2$ precursor, *RSC Adv.*, 2015, **5**, 68579–68586.

49 S. E. Atanasov, B. Kalanyan and G. N. Parsons, Inherent substrate-dependent growth initiation and selective-area atomic layer deposition of TiO$_2$ using "water-free" metal-halide/metal alkoxide reactants, *J. Vac. Sci. Technol., A*, 2016, **34**, 01A148.

50 M. Iwanaga, M. Watanabe and T. Hayashi, Charge separation of excitons and the radiative recombination process in PbBr$_2$ crystals, *Phys. Rev. B: Condens. Matter Mater. Phys.*, 2000, **62**, 10766–10773.

51 M. Jerman, Z. Qiao and D. Mergel, Refractive index of thin films of SiO$_2$, ZrO$_2$, and HfO$_2$ as a function of the films' mass density, *Appl. Opt.*, 2005, **44**, 3006.

52 G. Georgescu and A. Petris, Analysis of thickness influence on refractive index and absorption coefficient of zinc selenide thin films, *Opt. Express*, 2019, **27**, 34803.

53 K. Momma and F. Izumi, VESTA 3 for three-dimensional visualization of crystal, volumetric and morphology data, *J. Appl. Crystallogr.*, 2011, **44**, 1272–1276.

54 P. A. Beckmann, A review of polytypism in lead iodide, *Cryst. Res. Technol.*, 2010, **45**, 455–460.

55 C. Yang, X. Zhao, S. B. Kim, L. T. Schelhas, X. Lou and R. G. Gordon, Atomic layer deposition of cubic tin–calcium sulfide alloy films, *J. Mater. Res.*, 2020, **35**, 795–803.

56 E.-S. Park, C. Yoo, W. Kim, M. Ha, J. W. Jeon, T. Eom, Y. K. Lee and C. S. Hwang, Atomic Layer Deposition of Nanocrystalline-As-Deposited (GeTe)$_x$(Sb$_2$Te$_3$)$_{1-x}$ Films for Endurable Phase Change Memory, *Chem. Mater.*, 2019, **31**, 8752–8763.

57 J. J. P. M. Schulpen, M. A. Verheijen, W. M. M. Kessels, V. Vandalon and A. A. Bol, Controlling transition metal atomic ordering in two-dimensional Mo$_{1-x}$W$_x$S$_2$ alloys, *2D Mater.*, 2022, **9**, 025016.

58 S. C. Riha, A. A. Koegel, J. D. Emery, M. J. Pellin and A. B. F. Martinson, Low-Temperature Atomic Layer Deposition of CuSbS$_2$ for Thin-Film Photovoltaics, *ACS Appl. Mater. Interfaces*, 2017, **9**, 4667–4673.

59 M. J. S. Gynane, D. H. Harris, M. F. Lappert, P. P. Power, P. Rivière and M. Rivière-Baudet, Subvalent Group 4B metal alkyls and amides. Part 5. The synthesis and physical properties of thermally stable amides of germanium(II), tin (II), and lead(II), *J. Chem. Soc., Dalton Trans.*, 1977, 2004–2009.

60 M. Veith and M. Grosser, Cyclische Diazastannylene, XVI [1]. Ringe und Käfige mit Ge(II), Sn(II) und Pb(II)/ Cyclic Diazastannylenes, XVI [1]. Rings and Cages with Ge(II), Sn(II) and Pb(II), *Z. Naturforsch. B*, 1982, **37**, 1375–1381.

61 *APEX3 v2016.1-0*, Bruker AXS, Madison, Wisconsin, USA, 2016.

62 G. M. Sheldrick, SHELXT – Integrated space-group and crystal-structure determination, *Acta Crystallogr., Sect. A: Found. Adv.*, 2015, **71**, 3–8.

63 G. M. Sheldrick, Crystal structure refinement with SHELXL, *Acta Crystallogr., Sect. C: Struct. Chem.*, 2015, **71**, 3–8.

64 C. B. Hübschle, G. M. Sheldrick and B. Dittrich, ShelXle: a Qt graphical user interface for SHELXL, *J. Appl. Crystallogr.*, 2011, **44**, 1281–1284.

65 O. V. Dolomanov, L. J. Bourhis, R. J. Gildea, J. A. K. Howard and H. Puschmann, OLEX2: a complete structure solution, refinement and analysis program, *J. Appl. Crystallogr.*, 2009, **42**, 339–341.

66 M. Yoshimoto, T. Maeda, T. Ohnishi, H. Koinuma, O. Ishiyama, M. Shinohara, M. Kubo, R. Miura and A. Miyamoto, Atomic-scale formation of ultrasmooth surfaces on sapphire substrates for high-quality thin-film fabrication, *Appl. Phys. Lett.*, 1995, **67**, 2615.

67 D. Dumcenco, D. Ovchinnikov, K. Marinov, P. Lazić, M. Gibertini, N. Marzari, O. L. Sanchez, Y.-C. Kung, D. Krasnozhon, M.-W. Chen, S. Bertolazzi, P. Gillet, A. Fontcuberta i Morral, A. Radenovic and A. Kis, Large-Area Epitaxial Monolayer MoS$_2$, *ACS Nano*, 2015, **9**, 4611–4620.

68 R. A. Waldo, An Iteration Procedure to Calculate Film Compositions and Thicknesses in Electron-Probe Microanalysis, *Microbeam Anal.*, 1988, 310–314.

69 M. Ramsteiner, C. Wild and J. Wagner, Interference effects in the Raman scattering intensity from thin films, *Appl. Opt.*, 1989, **28**, 4017.

70 D. Yoon, H. Moon, Y.-W. Son, J. S. Choi, B. H. Park, Y. H. Cha, Y. D. Kim and H. Cheong, Interference effect on Raman spectrum of graphene on SiO$_2$/Si, *Phys. Rev. B: Condens. Matter Mater. Phys.*, 2009, **80**, 125422.

71 F. Neese, Software update: The ORCA program system—Version 5.0, *Wiley Interdiscip. Rev.: Comput. Mol. Sci.*, 2022, 1–15.

72 M. D. Hanwell, D. E. Curtis, D. C. Lonie, T. Vandermeersch, E. Zurek and G. R. Hutchison, Avogadro: an advanced semantic chemical editor, visualization, and analysis platform, *J. Cheminf.*, 2012, **4**, 17.

73 S. Ehlert, U. Huniar, J. Ning, J. W. Furness, J. Sun, A. D. Kaplan, J. P. Perdew and J. G. Brandenburg, r^{2}SCAN-D4: Dispersion corrected meta-generalized gradient approximation for general chemical applications, *J. Chem. Phys.*, 2021, **154**, 061101.

74 E. Caldeweyher, C. Bannwarth and S. Grimme, Extension of the D3 dispersion coefficient model, *J. Chem. Phys.*, 2017, **147**, 034112.

75 E. Caldeweyher, S. Ehlert, A. Hansen, H. Neugebauer, S. Spicher, C. Bannwarth and S. Grimme, A generally applicable atomic-charge dependent London dispersion correction, *J. Chem. Phys.*, 2019, **150**, 154122.

76 H. Kruse and S. Grimme, A geometrical correction for the inter- and intra-molecular basis set superposition error in Hartree-Fock and density functional theory calculations for large systems, *J. Chem. Phys.*, 2012, **136**, 154101.

77 R. M. Hanson, J. Prilusky, Z. Renjian, T. Nakane and J. L. Sussman, JSmol and the Next-Generation Web-Based

Representation of 3D Molecular Structure as Applied to Proteopedia, *Isr. J. Chem.*, 2013, **53**, 207–216.

78 G. A. Ozin, The single crystal Raman spectrum of orthorhombic $PbCl_2$, *Can. J. Chem.*, 1970, **48**, 2931–2933.

79 P. A. Temple and C. E. Hathaway, Multiphonon Raman Spectrum of Silicon, *Phys. Rev. B: Solid State*, 1973, 7, 3685–3697.

80 L. A. Isupova and E. V. Sobolev, Raman spectra of crystalline powders, *J. Struct. Chem.*, 1968, **9**, 263–265.